Assessment of Active and Hybrid Power Filters Under Space Vector Modulation

Man-Chung Wong, *Senior Member, IEEE*, Ying Pang, *Student Member, IEEE*, Zeng Xiang, *Member, IEEE*, Lei Wang, *Senior Member, IEEE*, and Chi-Seng Lam, *Senior Member, IEEE*

***Abstract*—Previous researches on space vector modulation (SVM) in active power filters (APFs) topologies find that compared with sinusoidal pulse width modulation, the SVM offers a better harmonic spectrum and has 15.47% more voltage utilization. The article not only proposes SVM for hybrid active power filters (HAPFs) but also answers the following questions. 1) Under what conditions both filters are equivalent to one another? 2) Which filter can enhance better tracking ability and better performance? 3) How the coupling component parameters and dc voltage affect the performance of both filters? The representative simulation and experimental results are given to verify the discussions. The conclusions can be application guidelines for the design of inductive and capacitive coupling inverters (e.g., APFs and HAPFs) in smart grids and development of energy internet due to their generalities to applications.**

***Index Terms*—Comparative error and loss analyses, dc voltage, hybrid active power filters (HAPFs), pulse width modulations (PWMs), space vector modulations (SVMs).**

NOMENCLATURE

A. Abbreviations

SVM	Space vector modulation.
PWM	Pulse width modulation.
CB	Capacitor bank.
PPF	Passive power filter.
APF	Active power filter.
HAPF	Hybrid active power filter.
SVC	Static Var compensator.
StatCom	Static synchronous compensator.
UPFC	Unified power flow controller.
TCLC	Thyristor-controlled *LC*.
THD	Total harmonic distortion.
PF	Power factor.
rms	Root mean square.
TCR	Tracking current ratio.
ESR	Equivalent series resistance.
IGBT	Insulated gate bipolar transistor.
QF	Quality factor.

B. Symbols

x	a, b, or c phase in three-phase system.
L, R	Coupling inductor and resistor of APF.
L_C, C_C, R_C	Coupling inductor, capacitor, and resistor of HAPF.
T_x, $\bar{T}_x$	Upper and lower IGBT in one arm.
V_{dc}, V_{Cdc}	DC capacitor voltage of the APF and HAPF, respectively.
C_{dc}, C_{Cdc}	DC capacitor of APF and HAPF, respectively.
s_x	Switching states of IGBT.
p, q	Load active and reactive powers.
i_{sx}, iLx, i_{cx}, i_{Ccx}, I_{cx}, I_{Ccx}	Source current, load current, injected compensating currents from the APF and from HAPF and their corresponding rms values, respectively.
i^*_{sx}, i^*_{cx}, i^*_{Ccx}	Reference source current, compensating currents from the APF and from HAPF.
v_{Lx}, v_{Rx}	Coupling inductor and resistor voltages in APF, respectively.
v_{CLx}, v_{CCx}, v_{CRx}	Coupling inductor, capacitor, and resistor voltages in HAPF, respectively.
v_{sx}, v_{inv}, v_{Cinvx}, V_{sx}, V_{invx}, V_{Cinvx}	Coupling point system voltage, inverter voltages of APF and HAPF, and their corresponding RMS values respectively.
T, K	Digital sampling period or switching time and the sampling instant.

Manuscript received March 4, 2020; revised May 20, 2020 and July 18, 2020; accepted August 16, 2020. Date of publication August 19, 2020; date of current version October 30, 2020. This work was supported in part by Macau Science and Technology Development Fund (FDCT, Macao) under Project FDCT 0026/2019/A1, in part by the University of Macau under Projects MYRG2017-00038-FST and MYRG2018-00056-FST, and in part by the State Key Laboratory of Internet of Things for Smart City of University of Macau. Recommended for publication by Associate Editor H. Ginn. *(Corresponding author: Lei Wang.)*

Man-Chung Wong, Ying Pang, and Zeng Xiang are with the State Key Laboratory of Internet of Things for Smart City, University of Macau, Macao 999078, China, and also with the Department of Electrical and Computer Engineering, Faculty of Science and Technology, University of Macau, Macao 999078, China (e-mail: mcwong@um.edu.mo; yb87446@um.edu.mo; yb57435@umac.mo).

Lei Wang is with the College of Electrical and Information Engineering, Hunan University, Changsha 410000, China (e-mail: jordanwanglei@hnu.edu.cn).

Chi-Seng Lam is with the State Key Laboratory of Analog and Mixed-Signal VLSI, University of Macau, Macao 999078, China,with the Institute of Microelectronics, University of Macau, Macao 999078, China, and also with the Department of Electrical and Computer Engineering, Faculty of Science and Technology, University of Macau, Macao 999078, China (e-mail: cslam@um.edu.mo).

Color versions of one or more of the figures in this article are available online at https://ieeexplore.ieee.org.

Digital Object Identifier 10.1109/TPEL.2020.3017750

$i_{cx}(0)$, $v_{CCx}(0)$, $i_{Ccx}(0)$	Initial APF coupling inductor current, initial HAPF coupling capacitor voltage, and inductor current, respectively.
I_{Ccmax}, I_{CM}, I_{CN}	HAPF maximum injected current, maximum collector current, and rated collector current, respectively.
ε	HAPF current slope change rate or acceptance non-linearity.
t_{cr}, t_{cr0}, t_{on}, t_{off}	The critical switching time, the critical switching time when all initial conditions are ignored correspondingly, switching turn-on time and turn-off time.
f, f_s, f_{sw}, f_{cr}, f_{cr0}	The *LC* coupling resonance frequency, system frequency, switching frequency, the critical switching frequencies corresponding with and without initial conditions, respectively.
i_{cex}, i_{Ccex}	The current difference between i_{cx} and i^*_{cx} and, the current difference between i_{Ccx} and i^*_{Ccx}, respectively.
$P_{loss(sw)}$, $P_{loss(L)}$, $P_{loss(LC)}$, $P_{loss(CC)}$	Switching loss, component conduction power losses of coupling L, L_C, and C_C.
K_e, K_{loss}, K_{TCR}	Ratio of error, power loss, and tracking current ratio between APF and HAPF.

I. Introduction

THE uses of APFs to mitigate reactive current and harmonic problems have drawn much attention since the 1970s [1]. For the sake of reducing power filters cost, HAPFs are developed, which combine active inverters and/or CBs, PPFs, and SVCs, and allow high power applications with reduced initial, operation, and maintenance costs. These active power compensators are all controlled by PWMs. In the PWMs control processes, the reference compensating current values are transferred to the IGBTs trigger turn-ON and turn-OFF signals [2].

Different PWMs are developed in [3]–[18] for controlling APFs and HAPFs. PWMs can be divided into two categories, unfixed switching frequency PWMs [3]–[9] and fixed switching frequency PWMs [10]–[14]. In the unfixed switching frequency PWMs, the carrier frequencies are varying. These PWMs can apply with the phase-shifting control [3], [4], fuzzy control [5], or soft-switching method [6] to reduce the switching loss. The hysteresis PWM as one of the representative unfixed switching frequency PWMs was first proposed in 1979, which is widely applied in power quality compensators. This method limits the compensating current within the hysteresis error bands [6]–[9]. The unfixed switching frequency PWMs have the advantage of relatively lower switching loss, but the switching ripples are difficult to filter out. In contrast, with fixed switching frequency PWMs [10]–[14], the ripples can be easily filtered out. Among fixed frequency PWMs, deadbeat PWM was discovered with the feedback control in 1996 [10], [11] to reduce error. However, it needs specially designed feedback control, which increases the control complexity. The classical SVM PWM was proposed in 1985, and its main purpose is to improve PWM dc voltage utilization [12]–[14]. In [14], it is stated that the upper limit of the phase-to-center voltage for the sinusoidal modulation is theoretically modulation to be 1. The maximum modulation index of SVM is 1.15 ($M = 2/\sqrt{3}$), which is larger than the conventional sinusoidal PWM modulation ($M = 1$). The flat-top SVM was developed in 2009 [15] to reduce the loss of the classical SVM.

However, all the above PWMs are based on inductive systems like APFs, StatComs [3]–[15]. Different from inductive systems, the capacitive systems normally have more complex coupling circuits such as LC-HAPFs [16]–[18] and TCLC-HAPFs [20], [21]. For the capacitive systems, the nonlinear hysteresis PWM and capacitive deadbeat PWM are proposed in [16]–[18], respectively. Specifically, an adaptive nonlinear hysteresis PWM is proposed in [16] for HAPFs to reduce switching loss and keep THD acceptable. In [17], the nonlinear current PWM characteristic is studied, in which nonlinear, quasi-linear, and linear operation regions are defined for the determination of the hysteresis band. In [18], an improved deadbeat control method is proposed for the HAPFs system with less steady-state error and fast dynamic response. All the above different PWMs algorithms [16]–[18] help capacitive compensators improve their performance, by increasing response speed and/or reducing the THD.

Table I is given to show the development of PWMs in APFs and HAPFs. It indicates that SVM is not investigated for controlling HAPFs, no matter it is classical or flat-top SVM. The advantages of classic SVM in APFs are high dc utilization and small steady-state error comparing to sinusoidal and hysteresis PWMs. In this article, it is an attempted trail to apply SVM in HAPFs.

APFs are inductive coupling impedance connecting with power electronic inverters, which are the general structures of flexible ac transmission devices, such as StatComs, SVGs, as well as UPFCs. Whereas HAPFs are capacitive coupling systems. Due to the lower operating dc voltages and lower losses comparing with inductive coupling inverter systems, HAPFs are further developed into such as the capacitive-coupling grid-connected inverters [19] and TCLC-HAPFs [20], [21] to inject active power as well as reactive power and to enhance high power quality in a grid. As a result, capacitive coupling inverter systems can be used to improve inductive coupling inverters performance, for example, reducing loss and system rating. Their studies are essential for smart grid development.

In Table II, there are several review papers [22]–[29] for APFs and HAPFs, which show that almost all of them are concerning configurations, topologies, ratings, controls, applications, etc. However, the below three questions are not included among existing literatures.

1) Under what conditions are two filters equivalent?
2) Which filter has better tracking ability or/and better performance?
3) How the coupling parameters and dc voltage affect the performances?

TABLE I
PWM COMPARISONS IN APFS AND HAPFS

PWM		Hysteresis	Deadbeat	SVM	
				Classical SVM	Flat-top SVM
APF	First proposed	1979	1996	1985	2009
	Ref.	[6]-[9]	[10], [11]	[12]-[14]	[15]
HAPF	First proposed	2012	2019	This work	
	Ref.	[16], [17]	[18]	-	-
Complexity		Simple	Complicated	Complicated	Complicated
Fixed f_{sw}		No	Yes	Yes	No

TABLE II
SUMMARY OF EXISTING REVIEW RESEARCH WORKS FOR APFS AND HAPFS

Filter Type	Reference	Year	Aspects and Features
APF	[22]	1999	Configurations, controls, and applications
APF	[23]	2000	Classifications by ratings, configurations, connections, compensation variables, controls, and references
HAPF	[24]	2003	Structures, transfer functions, and designs
HAPF	[25]	2008	Review of existing HAPF topologies and their transfer functions
APF and HAPF	[26]	2008	Applications of different topologies and corresponding applications
HAPF	[27]	2013	Topologies and Controllers
HAPF	[28]	2015	Structures and operation functions
HAPF	[29]	2018	Ranges, costs, reliabilities, and power losses

Due to the smart grid development, there are many types of research focusing on low cost, low loss, high efficiency, and multifunction inverters for microgrids. At this moment, most of them are inductive coupling inverters, while the capacitive coupling inverters are seldom discussed. Therefore, the pros and cons of both inverters are discussed, compared, and summarized in the article. Furthermore, to the best knowledge of authors' understanding, it is the first investigation to apply SVM in HAPFs.

The contributions of this article are summarized as follows.

1) Develop SVM for HAPFs.
2) Compare SVM differences between APFs and HAPFs in terms of
   a) maximum injected current in a switching period;
   b) dc operating voltage under the same injected current;
   c) nonlinear current operation characteristics;
   d) error under overmodulation and undermodulation;
   e) power loss;
   f) dynamic tracking ability.

Through comparing APFs and HAPFs, HAPFs SVM limitations and operational boundaries are discussed in terms of maximum injected current, determination of dc operating voltage, and switching frequency. Operational differences are compared through error performance, power loss, and dynamic tracking ability. Based on those, this article provides engineers with the inductive (APFs) and capacitive (HAPFs) coupling inverters application guidelines for the design of inductive and capacitive coupling inverters in smart grid development.

The layout of this article is as follows. In Section II, the mathematical model of SVM is provided for APFs and HAPFs. In Section III, comprehensive comparisons between inductive coupling systems (APFs) and capacitive coupling systems (HAPFs) are given to address the above questions. Experimented results are provided in Section IV to verify the results. The conclusion and application guidelines are summarized in Section V. Finally, flat-top SVM, influences of coupling components variation, compensating, and reference currents in experiments are provided in Section VI. An appendix is finally given before the References.

II. APF AND HAPF CIRCUIT CONFIGURATIONS AND SPACE VECTOR MODULATIONS

Fig. 1 illustrates the circuit configuration of the two-level three-phase three-wired APF or HAPF when the coupling impedance is inductive or capacitive, respectively. In Fig. 1, "Ground" is given in the figure as the zero-voltage reference.

A. Inverters Instantaneous Voltage Space Vectors and Compensating Currents

To control the IGBT turn-ON and turn-OFF states, switching function s_x is employed as (1).

$$s_x = \begin{cases} 1, \text{ when } \mathrm{T}_x \text{ are open, } \bar{\mathrm{T}}_x \text{ are closed} \\ -1, \text{ when } \mathrm{T}_x \text{ are closed, } \bar{\mathrm{T}}_x \text{ are open.} \end{cases} \tag{1}$$

By taking Park transformation [16], the instantaneous voltage vector can be transferred from a-b-c frame into α-β frame as given in (2), where $B = \{\vec{n}_\alpha, \vec{n}_\beta\}$ is a space base to spin with

$$\vec{v}_{invx} = V_{dc}\left[\sqrt{\frac{2}{3}}\left(S_a - \frac{1}{2}S_b - \frac{1}{2}S_c\right)\vec{n}_\alpha + \frac{1}{\sqrt{2}}\left(S_b - S_c\right)\vec{n}_\beta\right]. \tag{2}$$

A mixed coordinate instantaneous compensation [16], [17] is used. Its instantaneous active power p of the load can be determined by (3). Equation (4) shows the instantaneous injected reference current from the power filter, where $B' = \{\vec{n}_a, \vec{n}_b, \vec{n}_c\}$is a base in *a-b-c* frame. The *B* and *B'* can be transferred from one to another by (5). The time function of current to be compensated (i^*_{cx}) is defined, which consists of reactive and harmonic power components. i^*_{cx} can be expressed as

$$p = v_{sa}i_{La} + v_{sb}i_{Lb} + v_{sc}i_{Lc} \tag{3}$$

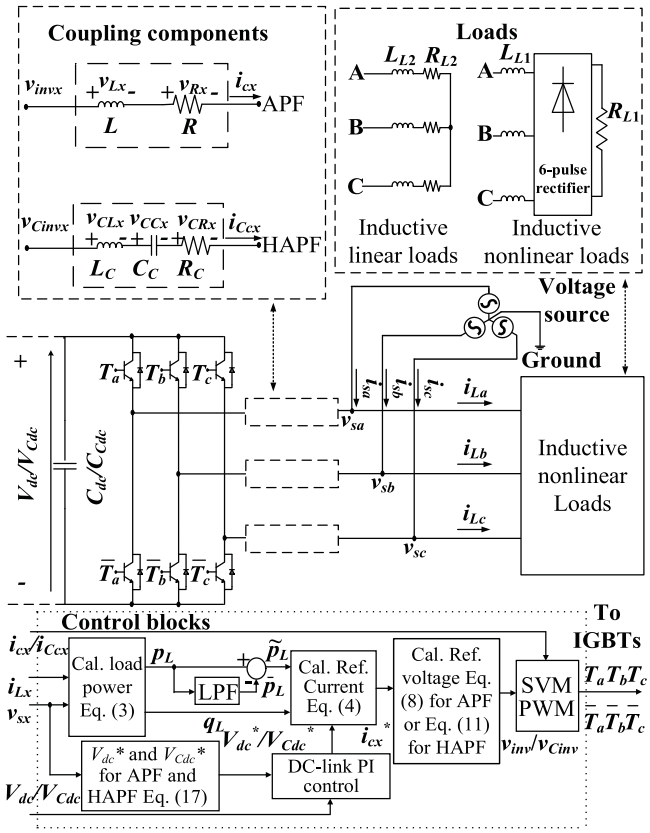

Fig. 1. Circuit configurations of the APF and HAPF.

$$\vec{i}_{cx}^{\,*} = \left(i_{La} - \frac{\bar{p}}{\Delta} v_{sa}\right)\vec{n}_a + \left(i_{Lb} - \frac{\bar{p}}{\Delta} v_{sb}\right)\vec{n}_b + \left(i_{Lc} - \frac{\bar{p}}{\Delta} v_{sc}\right)\vec{n}_c \tag{4}$$

where $\Delta = v_{sa}^2 + v_{sb}^2 + v_{sc}^2$, $\vec{n}_x$ is the per-unit vector, and $\bar{p}$ is the average value of p.

The intended compensation result (i_{sx}^*) is defined as only the average active component appears in source current i_{sx}. The reactive and harmonic components of the source current i_{sx} are compensated by controlling $i_{cx}\,(= i_{Lx} - i_{sx})$ to track its reference i_{cx}^*. The intended compensation result i_{sx}^* can be expressed as

$$\begin{bmatrix} i_{sa}{}^* \\ i_{sb}{}^* \\ i_{sc}{}^* \end{bmatrix} = \begin{bmatrix} i_{La} \\ i_{Lb} \\ i_{Lc} \end{bmatrix} - \begin{bmatrix} i_{ca}{}^* \\ i_{cb}{}^* \\ i_{cc}{}^* \end{bmatrix} = \begin{bmatrix} i_{La} \\ i_{Lb} \\ i_{Lc} \end{bmatrix} - \sqrt{2/3} \begin{bmatrix} 1 & 0 \\ -1/2 & \sqrt{3}/2 \\ -1/2 & -\sqrt{3}/2 \end{bmatrix} \begin{bmatrix} i_{c\alpha}{}^* \\ i_{c\beta}{}^* \end{bmatrix}. \tag{5}$$

In (3)–(5), it can be seen that, if the $i_{cx}\,(= i_{Lx} - i_{sx})$ is exactly equal to its reference i_{cx}^*, the intended compensation result can be obtained as the source current i_{sx} contains only $\bar{p}$ component.

To carry out fair comparisons, in this article, the loads used for APF and HAPF are exactly the same. In experimental case studies, the six-pulse rectifier loads are constructed as Fig. 1 with harmonic and inductive reactive power. The six-pulse rectifier nonlinear loads are selected since they are widely used in speed-controlled dc motors, and steel hardening machines, etc. [30], [31].

For better understanding, the relationship among i_{ca} in APF and i_{Cca} in HAPF and their reference i_{ca}^*, the zoom-in waveforms of i_{ca} in APF, and i_{Cca} in HAPF and their reference i_{ca}^* in experiments are shown in Fig. 19.

B. Required Reference Voltage Vector of APF

Referring to Fig. 1 with APF consideration, its inverter voltage vector has the following relationship as given in

$$\vec{v}_{invx} = \vec{v}_{sx} + L\frac{d\vec{i}_{cx}}{dt} + R\vec{i}_{cx}. \tag{6}$$

The required inverter voltage vector by APF and its corresponding required injected compensating current are accordingly given in

$$\vec{v}_{invx}\,[KT] = \vec{v}_{sx}\,[KT] + \frac{R}{X}\left\{\vec{i}_{cx}^{\,*}\,[KT] - (1-X)\,\vec{i}_{cx}\,[KT]\right\} \tag{7}$$

where $X = 1 - e^{-(R/L)T}$. For simplicity, when $R = 0$, (7) can be expressed as

$$\vec{v}_{invx}\,[KT] = \vec{v}_{sx}\,[KT] + L\frac{\left\{\vec{i}_{cx}^{\,*}\,[KT] - \vec{i}_{cx}\,[KT]\right\}}{T}. \tag{8}$$

C. Required Reference Voltage Vector of HAPF

Referring to Fig. 1 with HAPF consideration, its inverter voltage vector has the following relationship as given in

$$\vec{v}_{Cinvx} = \vec{v}_{sx} + L_C\frac{d\vec{i}_{Ccx}}{dt} - \frac{1}{C_C}\int \vec{i}_{Ccx}dt + R_C\vec{i}_{Ccx}. \tag{9}$$

After solving (9) for getting inverter reference voltage vector based on its required compensated current, HAPF voltage vector can be expressed as

$$\vec{v}_{Cinvx}\,[KT] = \vec{v}_{sx}\,[KT] - \vec{v}_{CCx}\,[KT] + L_C\frac{\vec{i}_{Ccx}\,[KT]\,\omega_0 e^{-\delta T}\sin(\omega T - \beta) + \omega\vec{i}_{Ccx}^{\,*}\,[KT]}{e^{-\delta T}\sin\omega T} \tag{10}$$

where $\delta = \frac{R_C}{2L_C}$, $\omega = \sqrt{\frac{1}{L_C C_C} - \left(\frac{R_C}{2L_C}\right)^2}$, $\omega_0 = \sqrt{\delta^2 + \omega^2}$, and $\beta = \arctan(\omega/\delta)$. For simplicity, when $R_C = 0$, (10) can be expressed as (11). It should be noted that f_s is 50 Hz and $f = \omega/2\pi$

$$\vec{v}_{Cinvx}\,[KT] = \vec{v}_{sx}\,[KT] - \vec{v}_{CCx}\,[KT] + L_C\frac{-\vec{i}_{Ccx}\,[KT]\,\omega\cos(\omega T) + \omega\vec{i}_{Ccx}^{\,*}\,[KT]}{\sin\omega T}. \tag{11}$$

D. Space Vector Modulation

The SVM procedure consists of section selecting, decomposing into basic vectors, determining switching sequence and time

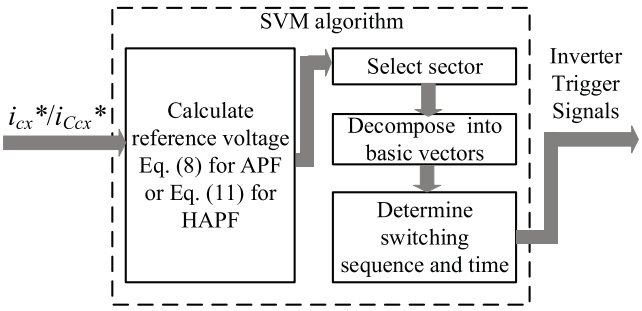

Fig. 2. Control block of SVM for APF or HAPF.

(from t_1 to t_6 depending on the determined basic vectors), and finally producing s_x switching states. The control block of SVM from reference current i^*_{cx} or i^*_{Ccx} to inverter trigger signals can be drawn as Fig. 2.

In three-phase two-level inverter SVM PWM, since zero vectors in eight different switches states do not affect the mean output voltage, the total duration of the zero states may be distributed in several ways. According to zero vectors distribution methods, it yields two types of equivalent modulation functions, resulting in two types of SVM.

1) In classic SVM [12], [13], each switch of the inverter is switched only once during one sampling interval.
2) In flat-top SVM [32], the zero vectors can be chosen freely (one time or more/less than one time during one sampling interval) to reduce the power losses.

In this article, the comparisons between APF and HAPF are provided under the same conditions. Therefore, classical SVM with the same fixed switching frequency is compared. In contrast, the flat-top SVM is analyzed under varying switching frequencies in Section VI.

III. Performance Comparisons Between APF and HAPF Under SVM PWM

In this section, APFs and HAPFs are comprehensively compared in terms of: 1) maximum injected current in a switching period; 2) dc operating voltage under the same injected current; 3) nonlinear current operation characteristics; 4) error under overmodulation and undermodulation regions; 5) power loss; and 6) dynamic tracking ability. The advantages and appropriate operational environments of APF and HAPF are concluded based on those comparisons.

A. Comparsion of Maximum Injected Current in a Switching

Figs. 3 and 4 show APF and HAPF voltage vectors and their corresponding compensating currents. Undermodulation region of SVM is defined when the targeted reference voltage is laid within the hexagon area bounded by space voltage vectors as shown in Fig. 3.

The injected current range of APF in one switching period can be calculated by

$$i_{cx} = \frac{1}{L}\int_0^T (v_{invx} - v_{sx})\,dt = \frac{v_{invx} - v_{sx}}{L}T. \tag{12}$$

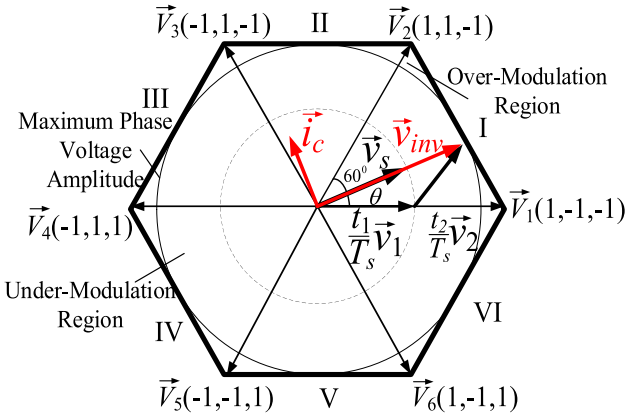

Fig. 3. APF vectors in SVM operation.

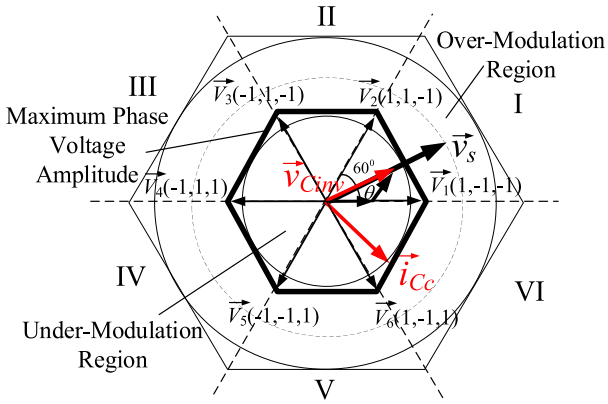

Fig. 4. HAPF vectors in SVM operation.

Comparing Figs. 3 and 4, current directions are different; one is leading voltage and another is lagging voltage. Equation (13) is the injected current by HAPF

$$i_{Ccx} = \left(\frac{v_{Cinvx} - v_{sx} + v_{CCx}(0)}{L_C\omega}\right)\sin(\omega t) + i_{Ccx}(0)\cos(\omega t)\,. \tag{13}$$

Unlike the injected current by an APF, the injected current by a HAPF consists of two oscillating sinusoid functions. Assuming all initial values are ignored, then its maximum injected current is

$$I_{Ccx\max} = (v_{Cinvx} - v_{sx} + v_{CCx}(0))\sqrt{\frac{C_C}{L_C}}. \tag{14}$$

The equivalent circuits for the APF and HAPF can be modeled, as shown in Fig. 5. In the APF, $V_{invx} > V_{sx}$. However, $V_{Cinvx} < V_{sx}$ in the HAPF. In the APF, the injected current is straightly increased due to its L coupling and $V_{invx} > V_{sx}$ within switching instant. On the other hand, the HAPF generates a sinusoidal current due to its LC coupling within switching instant. Unlike APF, in a switching period, HAPF current amplitude may not be linearly increased to the end of the switching period, which is controlled by LC resonance parameters as (14).

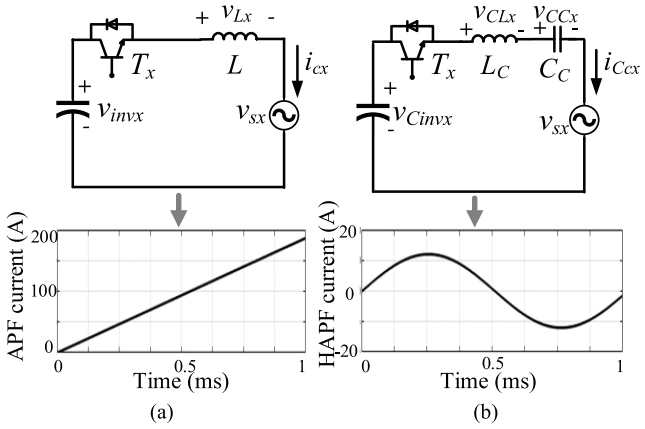

Fig. 5. Comparison of injected current between (a) APF and (b) HAPF under one period.

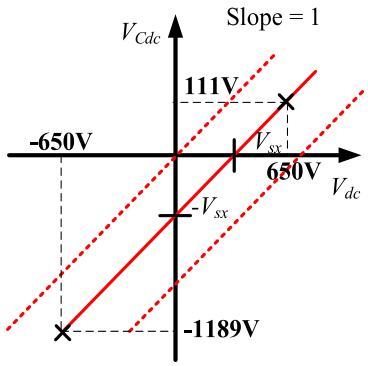

Fig. 6. DC voltage relationship between APF and HAPF.

B. DC Operation Voltage Under Same Injected Current

To compare an APF and a HAPF, the first step is to figure out what situations both systems can be equivalent to one another. Their compensating currents are assumed to be the same as (15), by referring (6) and (9)

$$i_{cx} = i_{Ccx} = \left(\frac{v_{invx} - v_{sx}}{L}\right) t = \left(\frac{v_{Cinvx} - v_{sx} + v_{CCx}(0)}{L_C \omega}\right) \sin(\omega t) + i_{Ccx}(0) \cos(\omega t) \tag{15}$$

where $R = R_C = 0$, $L = L_C$, and t is considered as an accumulated value. By simplification, (15) can be written as (16). For initial conditions, $v_{CCx}(0)$ is almost equal to v_{sx} and $i_{Ccx}(0)$ is zero. Considering line-to-line peak value and rms value, as a result, (16) can be expressed as (17)

$$v_{C\text{invx}} \approx v_{\text{invx}} - \left(v_{CCx}(0) + \frac{L i_{Ccx}(0)}{t}\right) \approx v_{\text{invx}} - v_{sx} \tag{16}$$

$$V_{Cdc} = V_{dc} - \sqrt{2} \cdot \sqrt{3} \cdot V_{sx}. \tag{17}$$

Fig. 6 shows the required dc voltage for APF in the horizontal axis and for HAPF in the vertical axis. In more general, Fig. 6 can link up the inductive and capacitive coupling inverters required dc voltage relationship.

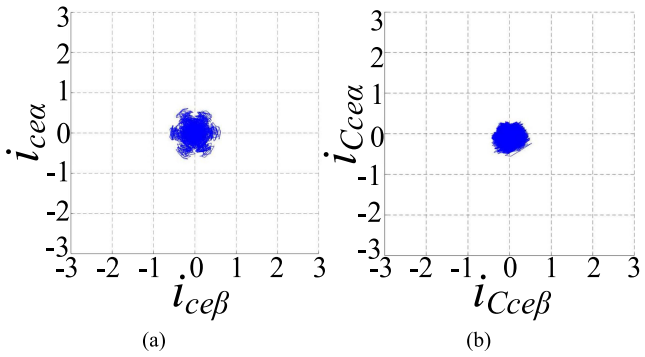

Fig. 7. Compensating current error in alpha-beta domain. (a) APF with 650 Vdc. (b) HAPF with 1189 Vdc.

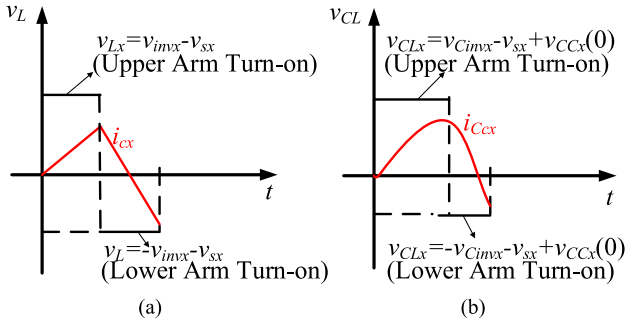

Fig. 8. Current slopes in (a) APF and (b) HAPF when switch changes states.

During the turn-OFF period, both V_{Cdc} and V_{dc} are negative, e.g., -650 V is required for APF, whereas -1189 V is required for HAPF when rms V_{sx} is 220 V. Therefore, when V_{Cdc} is set as 1189 V, HAPF can inject the same amplitude of current into the system comparing with an APF. The simulation proof is given in Fig. 7. APF and HAPF get almost the same shaded error area in the alpha-beta domain.

Fig. 6 is the theoretical outcome linking up the required dc voltage of an APF and a HAPF. It shows that when the coupling voltage is 220 V, an APF needs to use 650-V dc for the inverter to operate. However, that is equivalent to use 111 or 1189-V dc for a HAPF to operate. The system designer may choose either one of them to operate a HAPF. In order to reduce operation loss, the lower dc voltage should be chosen. Corresponding simulation and experimental results are given to show its validity by Figs. 7, 13, and 14.

C. Current Slope and Linearization

In the APF, the current slope is determined by the voltage between the coupling inductor as shown in (18) and Fig. 8(a)

$$\frac{di_{cx}}{dt} = \frac{v_{Lx}}{L} = \frac{v_{\text{invx}} - v_{sx}}{L}. \tag{18}$$

In the HAPF, the current slope in Fig. 8(b) is controlled by (19). APF current is linearly increased up to the end of the switching period as a linear straight line. However, HAPF current amplitude may not be linearly increased up to the end of

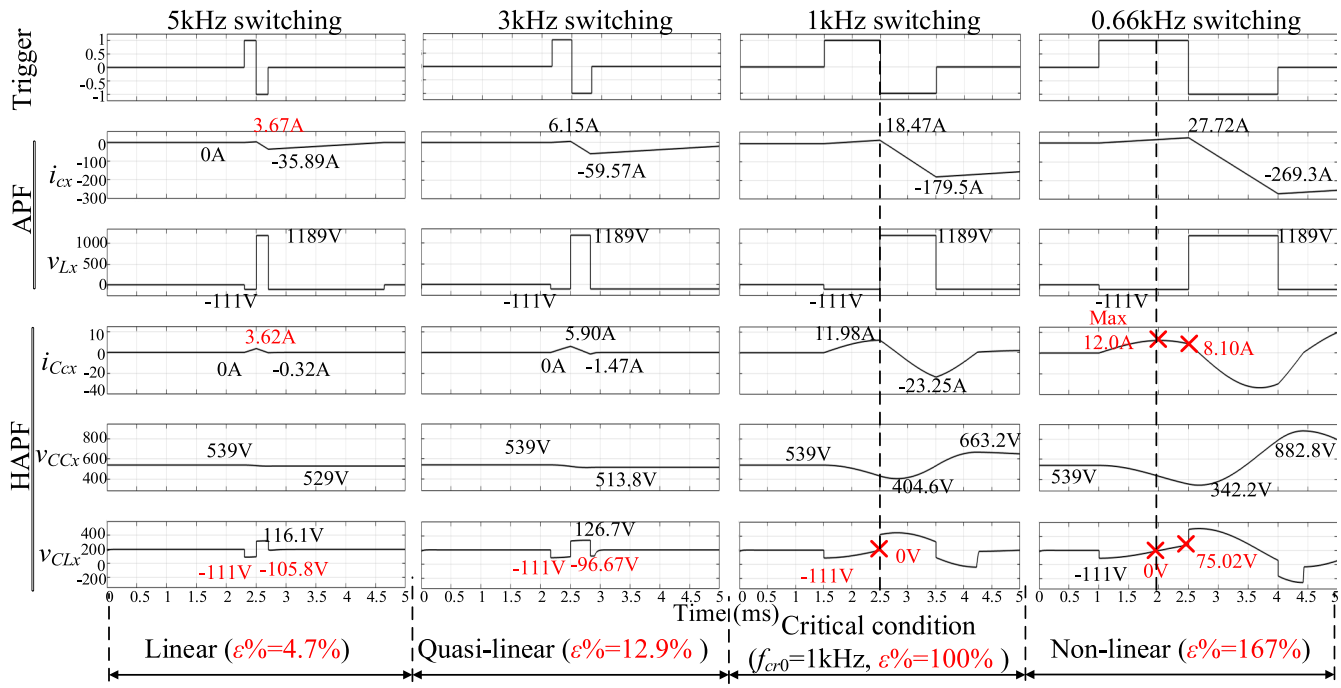

Fig. 9. Comparisons among i_{cx}, v_{Lx}, i_{Ccx}, v_{CCx}, v_{CLx} in different f_{sw} triggers using 5 kHz (linear), 3 kHz (quasi-linear), 1 kHz (critical), and 0.66 kHz (nonlinear).

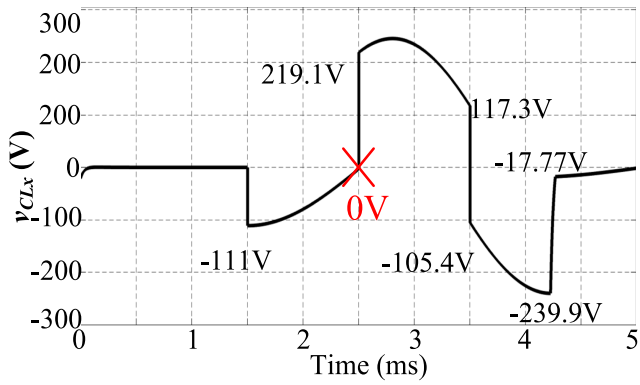

Fig. 10. v_{CLx} changes with switch states changing in critical condition.

the switching period. Therefore, HAPF operation modes can be classified into linear, quasi-linear, and nonlinear by its switching frequency

$$\frac{di_{Ccx}}{dt} = \frac{(v_{C\text{invx}} - v_{sx} + v_{CCx}(0))}{L_C}\cos\omega t - \frac{i_{Ccx}(0)}{\sqrt{L_C C_C}}\sin\omega t. \tag{19}$$

1) Critical Situation and Critical Switching Frequency: Fig. 9 shows the switching characteristics and their corresponding system parameters, in which v_{Lx} and v_{CLx} are coupling inductor voltages of the APF and the HAPF. Fig. 10 is an enlarged part of Fig. 9 at the critical case. It should be noted that the system line-line peak voltage is 539 V ($\sqrt{2}\cdot\sqrt{3}\cdot 220$ V). In Fig. 9, it is found that initial capacitor voltage $v_{CCx}(0)$ is almost equal to system line-line peak voltage.

In Fig. 10, the inductor voltage v_{CLx} shows a critical case from time 1.5 to 3.5 ms. In this critical case, the switch states of one HAPF arm changes from upper one turn-ON to lower one turn-ON at 2.5 ms. The current slope polarity is critical to be changed from positive to zero ($di_{Ccx}/dt = v_{CLx}/L_C = 0$) at 2.5 ms without switch states changing

$$\begin{aligned} t_{cr} &= t_{\max} \\ &= \sqrt{L_C C_C}\tan^{-1}\left(\frac{v_{C\text{invx}} - v_{sx} + v_{CCx}(0)}{i_{Ccx}(0)}\cdot\sqrt{\frac{C_C}{L_C}}\right). \end{aligned} \tag{20}$$

The critical switching time t_{cr} is defined when the slope of HAPF injected current is equal to zero, based on (19) in the article. When (19) equals 0, (20) can be obtained to calculate t_{cr}. Under this t_{cr}, the injected current reaches the maximum amplitude. At this condition, the switching frequency is defined as the critical switching frequency. After this t_{cr}, the injected current decreases, although it is a turn-ON situation, as shown in Figs. 9 and 10 after the cross signs. As a result, under such conditions, the PWM is out of control to reduce compensation error. Those out of control conditions are needed to be avoided in HAPF applications.

Table III summarizes the key equations and critical situations of the APF and HAPF.

In order to get a stable value, the inductor current $i_{cx}(0)$ and $i_{Ccx}(0)$ are taken out. The t_{cr} without initial influence can be defined as (21). Thus, in one switching period, its critical switching frequency f_{cr0} is defined in (22)

$$t_{cr0} = \frac{\pi\sqrt{L_C C_C}}{2} \tag{21}$$

$$f_{cr0} = \frac{2}{\pi\sqrt{L_C C_C}} = 4f. \tag{22}$$

TABLE III
KEY EQUATIONS COMPARISONS BETWEEN APF AND HAPF BY INJECTED CURRENT

	APF	HAPF
Injected current	$\frac{v_{invx} - v_{sx}}{L} T$	$\left(\frac{v_{Cinvx} - v_{sx} + v_{CCx}(0)}{L_C \omega}\right) \sin(\omega t) + i_{Ccx}(0) \cos(\omega t)$
Slope/derivatives	$(v_{invx} - v_{sx}) / L$	$\frac{(v_{Cinvx} - v_{sx} + v_{CCx}(0))}{L_C} \cos \omega t - \frac{i_{Ccx}(0)}{\sqrt{L_C C_C}} \sin \omega t$
Critical Switching Time	NA	$\sqrt{L_C C_C} \tan^{-1}\left(\frac{v_{Cinvx} - v_{sx} + v_{CCx}(0)}{i_{Ccx}(0)} \cdot \sqrt{\frac{C_C}{L_C}}\right)$
Critical Switching Frequency	NA	$\frac{2}{\pi \sqrt{L_C C_C}}$

Notes: NA means not available, because no critical switching time and frequency exist in APFs.

As shown in Fig. 9, the APF part has a linear slope current with a positive slope when the upper switch of an arm is ON and negative slope when the lower switch is ON.

2) Linear Region and Linear Switching Frequency: For the nonlinearity situation, ε is defined as the change rate of current slope or nonlinearity of the current as given in (23), where $i_{Ccx}(t_1)$ is the current at the time that the switch changes its state, namely, at the beginning of the interval. In contrast, $i_{Ccx}(t_2)$ is the current at the end of the interval.

For simplicity, no initial voltage and current are considered. Under ε acceptance linearity, one can define the switching frequency for HAPF having a linear slope current, which is defined by (24)

$$\varepsilon = \left| \left(\frac{di_{Ccx}(t_2)}{dt} - \frac{di_{Ccx}(t_1)}{dt} \right) \Big/ \frac{di_{Ccx}(t_1)}{dt} \right| = |1 - \cos \omega t| \tag{23}$$

$$f_{sw} = \frac{2\pi f}{\cos^{-1}(1 - \varepsilon)}. \tag{24}$$

3) Quasi-Linear Region and Switching Frequency: The current slope of the HAPF inverter i_{Ccx} can be classified as "quasi-linear" if $5\% < \varepsilon < 100\%$. Its quasi-linear switching frequency can be defined by (24) when $\varepsilon \in (0.05, 1.00)$.

4) Nonlinear Region: The slope of the HAPF inverter i_{Ccx} can be treated as "nonlinear," if its slope or polarity changes from positive to negative or vice versa without changing switching states. In this region, the requirement is $\varepsilon\% \geq 100\%$. Moreover, the i_{Ccx} appears obviously bending when its switch frequency is lower than the critical switching frequency (22). In Fig. 9, when the upper arm switch is still turned ON, the polarity of i_{Ccx} with 0.66-kHz slope has already been changed from positive to negative before the trigger changed, which is shown in Fig. 9 with the cross signs in the nonlinear region.

Finally, several simulations are performed in Fig. 11 to summarize the compensation performance with different f_{sw}, such that HAPF can be operated under nonlinear, quasi-linear, and linear regions with different f_{sw}. It can be found that performance has been improved from low to high f_{sw}.

Fig. 11 shows the HAPF characteristics of nonlinearity. The uncontrollable PWM current tracking reference operation cannot occur in an APF within a switching period, but it happens in HAPF when f_{sw} is too low, and it cannot be controlled to track reference.

D. Error

The analyses are based on general equivalent models of inductive and capacitive coupling systems, as shown in Fig. 5. Related simulation and experimental results are given to show their validity. However, the values for error ratio, power loss ratio, and tracking ability ratio are varied case by case due to the changing of the system parameters. However, their performance trends can be concluded by these analyses.

The comparison results of error between APF and HAPF are concluded based on the conditions that APF and HAPF are operated both in overmodulation or undermodulation conditions.

When (17) is fulfilled, the HAPF equivalent currents can be considered under two cases: Turn-ON (111 V) and turn-OFF (1189 V) situations. Under the equivalent turn-OFF case, it requires a higher dc voltage, which is not preferable and favorable.

Fig. 12 shows current waveforms i_{cx} for APF, i_{Ccx}, and i_{Cccx} for HAPF, where i_{cx} is the APF current, i_{Ccx} and i_{Cccx} are the HAPF currents at lower dc voltage and higher dc voltage, respectively. In Fig. 12, i_{Cccx} represents the turn-OFF case for HAPF, which requires a higher dc voltage. As a result, the current i_{Cccx} has a higher capability to track i_{cx} current at t_{LL}. i_{Ccx} is the HAPF current with lower dc voltage. There are points *a, b*, and *c* at t_1 for error analyses. The error is defined as the difference between i_{cx} (i_{Ccx}) and the targeted reference currents i_{cx}^* (i_{Ccx}^*) in (25) and (26), respectively. Considering the practical applications, the HAPF is selected to operate at the lower equivalent voltage to reduce the loss and cost. Thus, only the i_{Ccx} is analyzed below

$$i_{\text{cex}} = i_{cx} - i_{cx}{}^* = \frac{1}{L} (v_{\text{invx}} - v_{\text{invx}}{}^*) T \tag{25}$$

$$\begin{aligned} i_{Ccex} &= i_{Ccx} - i_{Ccx}{}^* \\ &= \frac{1}{L_C} (v_{C\text{invx}} - v_{C\text{invx}}{}^*) \sqrt{\frac{C_C}{L_C}} \sin(\omega T). \end{aligned} \tag{26}$$

Case 1. Equivalence: Case 1 occurs when the dc voltages of HAPF and APF are satisfied (17) under the linearization switching situation, as stated in (24). As shown in Fig. 12 before the t_L time, the ability to produce injected current by

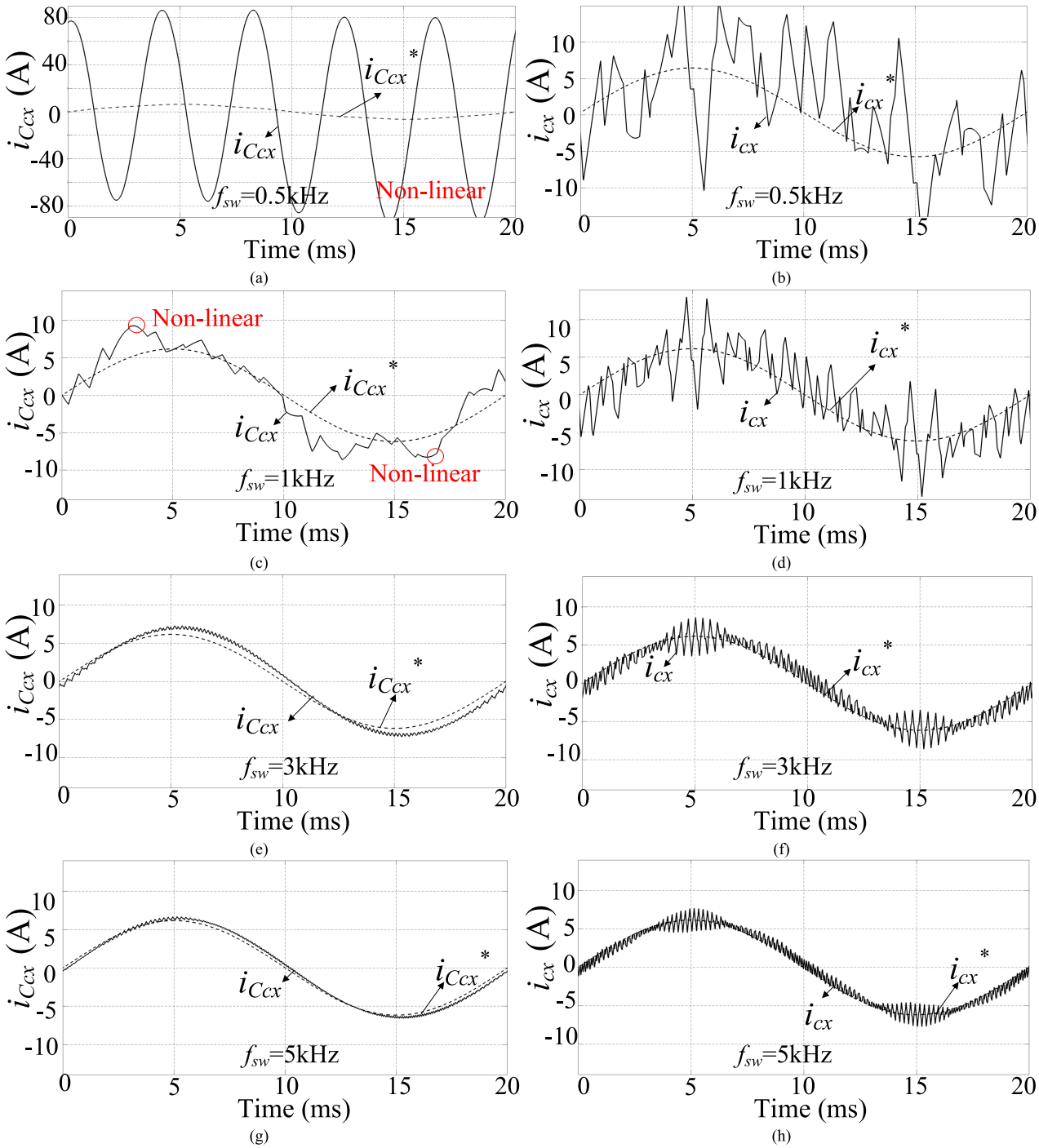

Fig. 11. Comparative waveforms of tracking current i_{cx} or i_{Ccx} and its sinusoidal reference i^*_{cx} (i^*_{Ccx}). (a) HAPF with $f_{sw} = 0.5$ kHz (nonlinear). (b) APF with $f_{sw} = 0.5$ kHz. (c) HAPF with $f_{sw} = 1$ kHz (critical). (d) APF with $f_{sw} = 1$ kHz. (e) HAPF with $f_{sw} = 3$ kHz (quasi-linear). (f) APF with $f_{sw} = 3$k Hz. (g) HAPF with $f_{sw} = 5$ kHz (linear). (h) APF with $f_{sw} = 5$ kHz.

APF and HAPF can be treated the same. Therefore, in this case, $i_{cx} = i_{Ccx}$ by ignoring all initial conditions during switching. There is no compensation performance difference between APF and HAPF. The simulation results are given in Fig. 7 and Fig. 11(g) and (h).

Case 2. Both Undermodulation (Point a): Case 2 occurs when a is the targeted reference. Both APF and HAPF can generate the targeted current at t_1. By referring Fig. 12, APF can generate a larger current (i_{cx}) difference comparing to HAPF current (i_{Ccx}) because HAPF injects nonlinear slope current, whereas APF current is linear. As a result, HAPF has a better performance in undermodulation.

Case 3. Under and Overmodulation (Point b): Case 3 occurs when point b is the targeted reference. The APF is in the undermodulation region, whereas HAPF is in overmodulation at t_1 with a lower dc voltage (turn-ON) case. APF has enough

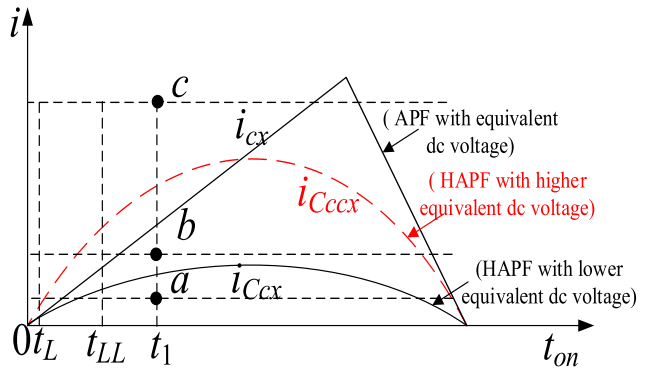

Fig. 12. Currents comparison between APF and HAPF.

capacity to track the current by SVM as a result. The tracking ability by APF in undermodulation region is better than HAPF under the overmodulation case. After several step operations, HAPF may turn from the overmodulation (Case 3) into the undermodulation region (Case 2) (Case 3→Case2).

Case 4. Both Overmodulation (Point c): Case 4 occurs when point c is the targeted reference. Both APF and HAPF currents cannot be generated within a switching period to such a high level at t_1. However, the difference between APF and HAPF is the amplitudes of the current, and the HAPF one is smaller. When dc voltage of HAPF is not enough, HAPF i_{Ccx} cannot reach point c. The tracking ability of APF is better than HAPF as i_{cx} is nearer to point c. However, as discussed in the above cases, after several steps of operations, HAPF may turn the cases from overmodulation into undermodulation situations (Case4→ Case 3→Case 2)

$$K_e = \frac{\frac{1}{T}\int |i_{cex}|\,dt}{\frac{1}{T}\int |i_{Ccex}|\,dt} = \frac{\frac{1}{T}\int \frac{1}{L}\,|v_{invx} - v_{inv}{}^*|dt}{\frac{1}{T}\int \frac{1}{L_C}\left|(v_{Cinvx} - v_{Cinv}{}^*)\sqrt{\frac{C_C}{L_C}}\sin(\omega T)\right| dt} \tag{27}$$

$$K_e \approx \frac{L_C}{L}\frac{\int |V_{dc} - v_{inv}{}^*|\,dt}{\int \left|V_{dc} - \sqrt{6}V_{sx} - v_{Cinv}{}^*\right| dt}. \tag{28}$$

In summary, all modulation conditions can be summarized as a procedure starting from overmodulation and into undermodulation or directly starting from undermodulation. To further compare their error performances, an error ratio between the average absolute current difference of APF and HAPF in a cycle is defined as K_e and given in (27). By referring (17) into (27), it can be simplified as (28). When $K_e > 1$, HAPF performance is better than APF.

Table IV is a simulation summary for K_e, in which APF is operating with 650 V dc voltage at 10 kHz switching frequency, whereas HAPF is with 111 V dc voltage at 10 kHz. It shows that HAPF has a better compensation performance than APF about 3.81 times when the same coupling inductors are taken. However, its compensation performance can be further adjusted by taking different coupling inductance values. If the L_C is chosen as two times of L, the K_e will increase to 6.95 times,

TABLE IV
ERROR RATIOS COMPARISONS WITH DIFFERENT COUPLING INDUCTORS

	L=L_C=6mH	L=3mH, L_C=6mH	L=6mH, L_C=3mH
$\frac{1}{T}\int\|i_{cex}\|dt$ (A)	0.122	0.224	0.122
$\frac{1}{T}\int\|i_{Ccex}\|dt$ (A)	0.032	0.032	0.062
K_e	3.81	6.95	1.97

TABLE V
QUALITY FACTOR AND ESR OF APF AND HAPF

	Parameters	Physical values
APF	L	6mH (QF=18, ESR_L=0.09Ω)
HAPF	L_C, C_C	6mH (QF=18, ESR_{LC}=0.09Ω), 70μF (QF=170, ESR_{CC}=0.11Ω)

Notes: QF stands for the quality factor, and *ESR* stands for equivalent series resistance.

and when L_C is chosen as half of L, the K_e will reduce to 1.97 times.

E. Power Loss

Less operating dc voltage means less power loss. As a result, it is suggested that HAPF should be operated in consideration of turn-ON mode so that less dc voltage can be taken, as shown in the first quadrant of Fig. 6.

According to the power loss studies, the switching loss [29], [35], and the component conduction loss [36], [37] contribute to the major power loss of the system.

1) Switching Loss: The switching loss of the switching device can be classified as turn-ON and turn-OFF losses. Equation (29) is the total turn-ON and turn-OFF power losses.

Thus, the higher of the V_{dc}, V_{Cdc}, and f_{sw} of the APF and HAPF, the higher the switching loss is obtained and vice versa

$$P_{\text{loss}(sw)} = V_{dc}I_{\text{loss}} = V_{dc}I_{CM}f_{sw}\left(\frac{1}{8}t_{on}\frac{I_{CM}}{I_{CN}} + t_{off}\left(\frac{1}{3\pi} + \frac{1}{24}\frac{I_{CM}}{I_{CN}}\right)\right). \tag{29}$$

2) Component Conduction Loss: For APF, the component conduction power loss of coupling inductor can be expressed as

$$P_{\text{loss}(L)} = ESR_L \cdot I_{cx}^2. \tag{30}$$

For HAPF, the component conduction power loss of coupling inductor and coupling capacitor can be expressed as

$$P_{\text{loss}(L_C)} = ESR_{L_C} \cdot I_{Ccx}^2 \tag{31}$$

$$P_{\text{loss}(C_C)} = ESR_{C_C} \cdot I_{Ccx}^2 \tag{32}$$

where ESR_L/ESR_{LC} and ESR_{CC} are equivalent series resistance of coupling inductor L/L_C and coupling capacitor C_C, respectively. According to the measurement results, the *QF* and *ESR* of APF and HAPF are given in Table V. Tables VI–VIII below summarize the switch power loss, component conduction power loss, and the total power losses of APF and HAPF in simulations, respectively.

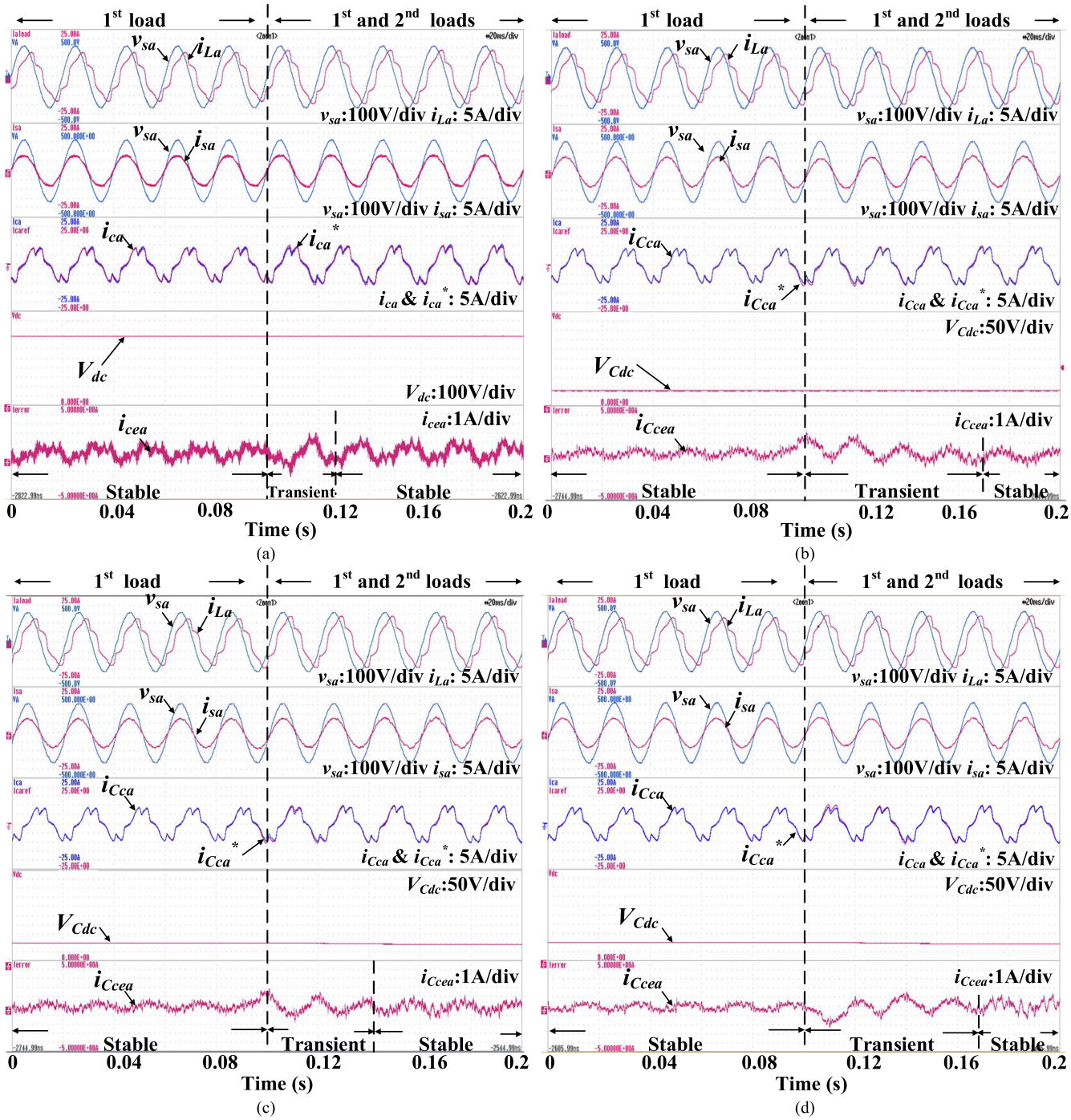

Fig. 13. Waveforms of load voltage, load current, source current, reference current, compensating current, dc voltage, and error current, before and after load case changed from first load to first and second loads compensated by: (a) APF ($f_{sw} = 10$ kHz, $L = 6$ mH); (b) HAPF ($f_{sw} = 5$ kHz, $L_C = 6$ mH); (c) HAPF ($f_{sw} = 10$ kHz, $L_C = 3$ mH); (d) HAPF ($f_{sw} = 10$ kHz, $L_C = 6$ mH).

By combining power loss consideration in (29)–(32), it is obvious that the loss is proportional to dc voltage and switching frequency. The power loss ratio between $P_{loss(APF)}$ for APF and $P_{loss(HAPF)}$ for HAPF is defined as K_{loss} in (33)

$$K_{\text{loss}} = \frac{P_{\text{loss(APF)}}}{P_{\text{loss(HAPF)}}} = \frac{P_{\text{loss}(sw\text{APF})} + P_{\text{loss}(L)}}{P_{\text{loss}(sw\text{HAPF})} + P_{\text{loss}(L_C)} + P_{\text{loss}(C_C)}}. \tag{33}$$

F. Dynamic Tracking Ability

In this section, only undermodulation operations of APF and HAPF are considered. It means that enough dc voltage should be supported to APF and HAPF simultaneously following (17) dc voltage requirement. The dynamic tracking ability can be considered by the change rate of currents between APF and HAPF, and it is discussed as follows.

TABLE VI
SWITCHING LOSS OF APF AND HAPF IN SIMULATION

	DC voltage (V)	Switching Loss (W) (1st load)	Switching Loss (W) (1st and 2nd loads)
APF	650	84	142
HAPF	110	24	38

TABLE VII
COMPONENT CONDUCTION LOSS OF APF AND HAPF IN SIMULATION

	Component conduction loss (W) (1st load)	Component conduction loss (W) (1st and 2nd loads)
APF	4.4	5.7
HAPF	9.8	12.8

TABLE VIII
TOTAL POWER LOSS OF APF AND HAPF (SWITCHING LOSS AND CONDUCTION LOSS) IN SIMULATION

	Total power loss (1st load)	Total power loss (1st and 2nd loads)
APF	88.4W	147.7W
HAPF	33.8W	50.8W
K_{loss}	2.62	2.91

Comparing (19) and taking the first term of Taylor's series expansions for sin and cos functions, the change rate of current of a HAPF can be given in (34). The second term of (34) acts as a damping factor to reduce the change rate of current. The initial capacitor voltage $v_{CCx}(0)$ is near or equal to v_{sx}. It reduces the change rate of current

$$\frac{di_{Ccx}}{dt} = \frac{(v_{C\text{invx}} - v_{sx} + v_{CCx}(0))}{L_C} - \frac{i_{Ccx}(0)}{L_C C_C} t. \tag{34}$$

Then, its change rate of TCR comparing with APF can be given in (35). If it can fulfill (17), it can be further simplified into (36)

$$K_{\text{TCR}} = \frac{\frac{di_{cx}}{dt}}{\frac{di_{Ccx}}{dt}} \approx \frac{L_C}{L} \cdot \frac{v_{\text{invx}} - v_{sx}}{v_{C\text{invx}}} \tag{35}$$

$$K_{\text{TCR}} = \frac{L_C}{L}. \tag{36}$$

When K_{TCR} is equal to 1, it means that the dynamic tracking ability of APF and HAPF can be treated as the same.

A simulation is performed, and the results are shown in Fig. 14. It shows that when the L and L_C are the same as shown in Fig. 14(b), tracking current and ratio are the same. When the L or L_C is reduced to the half as shown in Fig. 14(a) or (c), the tracking current and ratio can be two times than before. Equation (36) defines the current tracking ability relationship between APF and HAPF. It shows that coupling inductors between APF and HAPF are the key to control the current tracking ability in undermodulation cases.

IV. EXPERIMENT RESULTS

In this section, a 220 V–5 kVA experiment prototype of APF/HAPF is built in the laboratory, as shown in Fig. 15, to provide experimental results and to verify the above discussions. The digital control system of APF/HAPF is a digital signal processor TMS320-F28335 controller. The switching devices for the inverter are Mitsubishi IGBT intelligent power modules PM300DSA060. Among these experimental results, waveforms are recorded by the YOKOGAWA DL850 oscilloscope. The power loss and THD are measured by YOKOGAWA WT1800 PRECISION ANALYZER and Fluke 435.

According to [16], [17], and (23), the f_{sw} for the HAPF is selected to be 10 kHz.

Hardware experimental components parameters and the test loadings are listed in Table IX. The experimental waveform results are shown in Fig. 13 includes transient and steady-state conditions from first load to first and second loads. Finally, the results are summarized in Tables X and XI.

Tables X and XI illustrate APF has faster tracking ability than HAPF with equivalent parameters, but HAPF has a less steady-state error, and K_e is 2.94 times (nearly three times). APF has the largest power loss, and K_{loss} with the same f_{sw} between APF and HAPF is 2.78 times (almost 3 times).

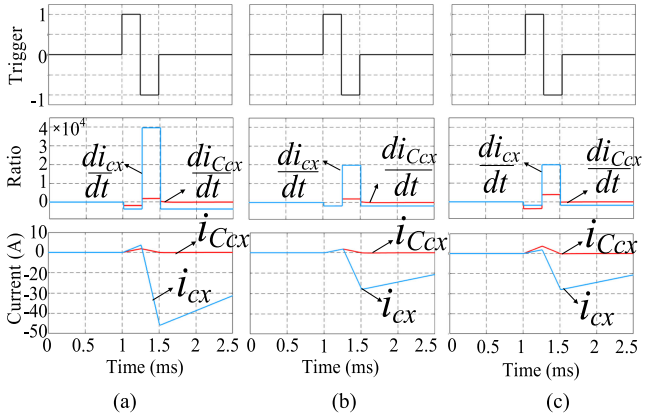

Fig. 14. Comparison between current and TCR. (a) $v_{inv} = 650$ V, $v_{Cinv} = 111$ V, $L = 3$ mH, $L_C = 6$ mH, $C = 70\,\mu$F; (b) $v_{inv} = 650$ V, $v_{Cinv} = 111$ V, $L = 6$ mH, $L_C = 6$ mH, $C_C = 70\,\mu$F; (c) $v_{inv} = 650$ V, $v_{Cinv} = 111$ V, $L = 6$ mH, $L_C = 3$ mH, $C_C = 70\,\mu$F.

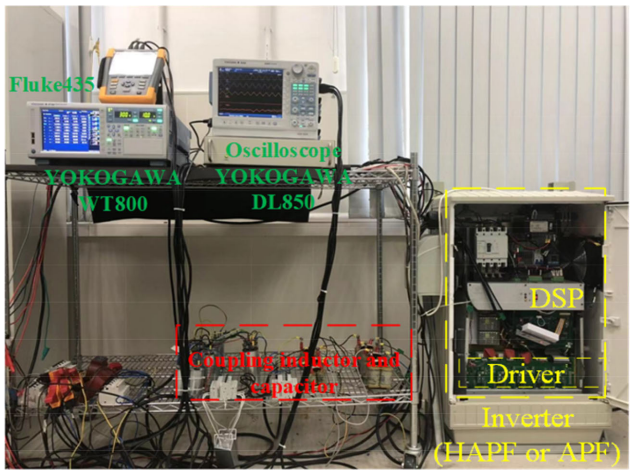

Fig. 15. Experimental hardware platform setup of the 5-kVA prototype of APF and HAPF.

TABLE IX
SIMULATION/EXPERIMENTAL PARAMETERS FOR APF AND HAPF

	Parameters	Physical values
Coupling parameters	L, C_C, L_C	6mH, 70μF, 6mH or 3mH
Load parameters	L_{L1}, R_{L1}, L_{L2}, R_{L2}	160mH, 110Ω, 700mH, 10Ω
System parameters	S, V_{sx}	8kVA, 220V
DC voltage	V_{dc}, V_{Cdc}	650V, 110V
Switching frequency	f_{sw}	5kHz, 10kHz
Load power quality	THD_{L1}, THD_{L2}, PF_{L1}, PF_{L2}	16.3%, 14.3%, 0.57, 0.53

TABLE X
EXPERIMENTAL RESULTS OF TWO SETS OF LOADS BEFORE AND AFTER COMPENSATION OF APF OR HAPF

		Q_s (Var)	P_s (W)	THD_{is} (%)	PF	P_{loss} (W)	$\frac{1}{T}\int\lvert i_{cea}\rvert dt$ (mA)	Tracking time (ms)
1st Load	Before Comp.	3310	2338	16.3	0.57	-	-	-
	APF (10kHz, 6mH)	104.1	2680	4.1	0.99	342	0.91	-
	HAPF (5kHz, 6mH)	115.3	2442	3.9	0.99	104	0.39	-
	HAPF (10kHz, 3mH)	126.7	2470	3.8	0.99	132	0.39	-
	HAPF* (10kHz, 6mH)	93.5	2461	3.1	0.99	123	0.31	-
1st and 2nd Load	Before Comp.	3980	2491	14.3	0.53	-	-	-
	APF (10kHz, 6mH)	115.8	2865	4.7	0.99	374	0.98	25
	HAPF (5kHz, 6mH)	127.5	2601	4.1	0.99	110	0.43	70
	HAPF (10kHz, 3mH)	138.2	2654	4.0	0.99	163	0.42	40
	HAPF* (10kHz, 6mH)	103.7	2645	3.5	0.99	154	0.39	70

**Notes:* Only the different parameters have been marked.

TABLE XI
RATIOS RELATIONSHIP BETWEEN CORRESPONDING COMPARATIVE FILTERS AND THE HAPF (10 kHz, 6 mH) IN EXPERIMENT

		Error ratio	Power loss	Tracking time
1st Load	APF (10kHz, 6mH)	2.94	2.78	-
	HAPF (5kHz, 6mH)	1.25	0.84	-
	HAPF (10kHz, 3mH)	1.25	1.07	-
	HAPF (10kHz, 6mH)	1	1	-
1st and 2nd Loads	APF (10kHz, 6mH)	2.51	2.43	0.36
	HAPF (5kHz, 6mH)	1.10	0.71	1
	HAPF (10kHz, 3mH)	1.08	1.06	0.57
	HAPF (10kHz, 6mH)	1	1	1

Notes: The shades areas mean outstanding results. Error ratio is defined by comparing the average absolute current difference in a cycle under steady-state situation and taking HAPF (10 kHz, 6 mH) compensation performance as the ratio relationship reference.

V. CONCLUSIONS AND APPLICATION GUIDELINES

In this article, several important characteristics and application guidelines between APF and HAPF are concluded as below.

1) HAPF voltage vector is given in (11), and its corresponding SVM in HAPF is proposed and verified by Figs. 11, 13, Tables X, and XI.
2) In a switching period, unlike APF, HAPF current amplitude may not be linearly increased up to the end of switching period, which is controlled by *LC* resonance parameters. Sometimes, under nonlinear situations, its amplitude will be decreased within a switching period. These phenomena are given in Figs. 5, 9, and 10.
3) The inductive-coupled inverter (like APF) and the capacitive-coupled inverter (like HAPF) can be equivalent to one another when dc voltage relationship in (17) is fulfilled. The required dc voltage of HAPF is about six times lower than APF, as verified by Figs. 7, 13, and Tables X and XI.
4) The critical switching frequency is defined by (22). If the switching frequency is lower than this critical value, the HAPF has a nonlinear current slope, which may worsen compensation performance. This critical switching frequency is verified by Figs. 9 and 11.
5) The HAPF switching operation modes can be classified into linear, quasi-linear, and nonlinear according to its current slope changing rate ε in (23). The HAPF is recommended to operate under quasi-linear or linear mode, as proved by Fig. 9.
6) When APF and HAPF are both in the overmodulation region, APF has better tracking ability. When APF and HAPF are in the undermodulation region, HAPF has better compensation performance and less steady-state error. HAPF is recommended to operate in undermodulation region, which is verified by Fig. 13 and Tables X and XI;
7) Power losses are affected by the dc voltage and switching frequency. The HAPF can choose to have lower dc voltage and lower switching frequency, as verified by Tables X and XI.
8) The coupling inductors in APF and HAPF affect not only the compensation performance but also the dynamic tracking ability by (28) and (36). With smaller coupling inductance, HAPF has better-tracking performance but larger steady-state error, as shown in Fig. 13 and Tables X and XI.

TABLE XII
COMPARISONS BETWEEN ADVANTAGES, DISADVANTAGES, AND CORRESPONDING OPERATIONAL ENVIRONMENTS OF APF AND HAPF

	Advantageous aspects	Disadvantages aspects	Appropriate operational environments
APF	Better tracking ability	Higher loss, larger compensation error	Load situations always change
HAPF	Lower loss, better compensation error	Lower tracking ability	Steady and stable load situations

APF and HAPF have their advantages and disadvantages. In general, APF has better tracking ability, but it has a higher loss and relatively larger compensation error. Thus, APF is suitable for the system with frequent load changing. On the other hand, HAPF has a lower loss and better compensation error. Therefore, HAPF is suitable to apply in a relatively steady and stable load system. Table XII expresses the advantages, disadvantages, and corresponding appropriate operational conditions of APF and HAPF. Besides, HAPF switching frequency, dc operating voltage, and system components should be determined accordingly in this article.

TABLE XIII
INFLUENCES OF COUPLING PARAMETERS VARIATION TO DIFFERENT ITEMS

System	Parameter increase	DC voltage	Maximum current	Critical switching frequency	Steady-state error	Tracking ability
APF	$L\uparrow$	Increase	No change	NA	Decrease	Decrease
	$R\uparrow$	Increase	Decrease	NA	Increase	Decrease
HAPF	$C_C\uparrow$	Increase	Increase	Decrease	Increase	Increase
	$L_C\uparrow$	Increase	Decrease	Decrease	Decrease	Decrease
	$R_C\uparrow$	Increase	Decrease	No change	Increase	Decrease

Notes: NA means not available, because no critical switching frequency exists in APFs.

VI. DISCUSSIONS

A. Parameters Influences

The influences of the parameters (*L*, *R*, C_C, L_C, and R_C) variation in the current error and in the overall control performance can be summarized by the aspects of V_{dc} (V_{Cdc}), I_{cmax} (I_{Ccmax}), critical switching frequency, steady-state error, and tracking ability. The analyses are all based on the functions of each above items from (37) to (42).

When *R* and R_C are considered, the V_{dc} and V_{Cdc} are calculated as follows:

$$V_{dc\min} = v_{invx\max} = v_{sx} + \frac{R}{X}\left\{{i_{cx}}^* - (1-X)\, i_{cx}\right\} \quad (37)$$

$$V_{Cdc\min} = v_{Cinvx\max} = v_{sx} - v_{CCx} + L_C \frac{i_{Ccx}\omega_0 e^{-\delta T}\sin(\omega T - \beta) + \omega {i_{Ccx}}^*}{e^{-\delta T}\sin\omega T} \quad (38)$$

where $X = 1 - e^{-(R/L)T}$, $\delta = \frac{R_C}{2L_C}$, $\omega = \sqrt{\frac{1}{L_C C_C} - \left(\frac{R_C}{2L_C}\right)^2}$, $\omega_0 = \sqrt{\delta^2 + \omega^2}$, and $\beta = \arctan(\omega/\delta)$.

When the *R* and R_C are considered, the current steady-state error functions are calculated as follows:

$$i_{cex} = i_{cx} - {i_{cx}}^* = \frac{1 - e^{-(R/L)T}}{R}\left(v_{invx} - {v_{invx}}^*\right) T \quad (39)$$

$$i_{Ccex} = i_{Ccx} - {i_{Ccx}}^* = \left(v_{Cinvx} - {v_{Cinvx}}^*\right)\frac{\sin(\omega T)\, e^{-\delta T}}{\omega L_C}. \quad (40)$$

Tracking ability is another aspect of performance, which respects the maximum current slope can be tracked. The compensating current slope can be expressed as follows:

$$\frac{di_{cx}}{dt} = e^{-\frac{R}{L}T}/L \cdot (v_{inv} - v_s) \quad (41)$$

$$\frac{di_{Ccx}}{dt} = e^{-\delta T}\frac{(v_{Cinvx} - v_{sx} + v_{CCx}(0))}{\omega L_C} \cdot (\omega\cos\omega T - \delta\sin\omega T) \quad (42)$$

Based on the deduced (37)–(42), the influences of the parameters (*L*, *R*, C_C, L_C, and R_C) variation in different corresponding items can be summarized in Table XIII.

B. Overmodualtion and Flat-Top SVM

1) Overmodulation: The modulation rate *M* for APF and M_C for HAPF are defined as the ratio between inverter voltage v_{invx} and the dc voltage V_{dc} (V_{Cdc}) as

$$M = v_{invx}/V_{dc} \quad (43)$$

$$M_C = v_{Cinvx}/V_{Cdc}. \quad (44)$$

According to the definition in SVM [33], when $0.907 < M(M_C) < 1$, the modulation is considered as overmodulation. When $0 < M(M_C) < 0.907$, it can be treated as undermodulation. When operating at undermodulation, a modulated voltage vector can reach its reference voltage. However, when the $0.907 < M(M_C) < 1$, since the modulated voltage cannot reach the reference, the $M(M_C)$ should be replaced by another one based on the overmodulation look-up table [34]. On the other hand, if APF and HAPF operate in SVM overmodulation region, the required voltage reference for compensation is close to or higher than dc voltage.

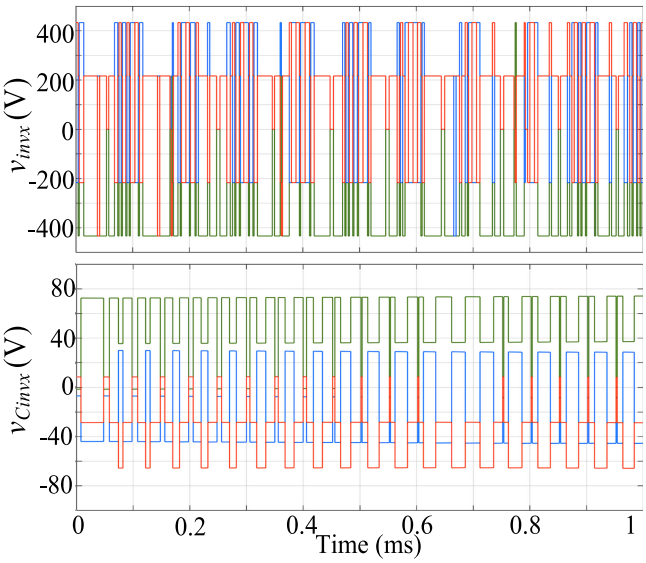

Fig. 16. Comparison between v_{invx} and v_{Cinvx} in the simulation.

As shown in Fig. 16, the v_{invx} for APF changes from +420 to −420 V, with the 65% maximum *M*. The v_{Cinvx} for HAPF changes from +75 to −75 V, with the 68% maximum M_C. Therefore, there is no overmodulation occurs in both APF and HAPF.

2) Flat-Top Modulation:: Since in SVM voltage vector is always synthesized by two neighboring voltage vectors, reference v^* can be expressed as

$$\vec{v}^* = t_k \cdot \vec{v}_k + t_{k+1} \cdot \vec{v}_{k+1} \quad (45)$$

where t_k is the turn-ON constant time of $\vec{v}_k$.

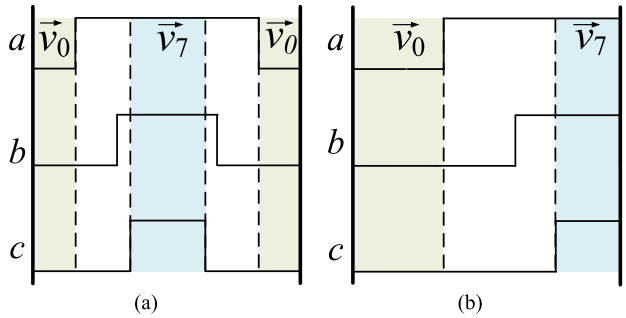

Fig. 17. Equivalent voltage vector output switch states. (a) Classical SVM. (b) Flat-top SVM.

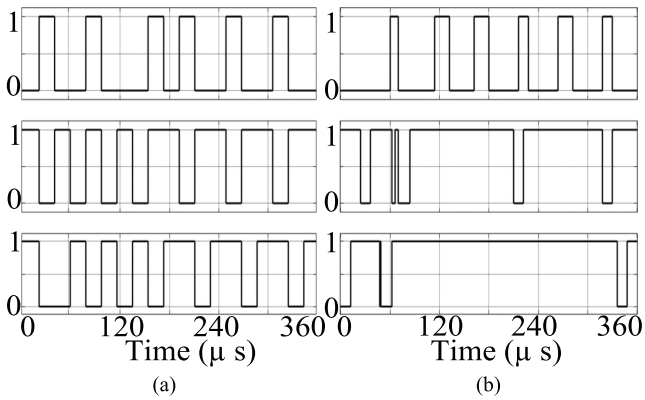

Fig. 18. Switch sequences comparison. (a) Classical SVM. (b) Flat-top SVM.

In classical SVM, each leg of the inverter must switch once in a period, which means every switching period must start with v_0 and end with v_0. v_7 appears in the middle. The time functions of every voltage vector constant time are arranged as

$$\begin{cases} T = t_0 + t_7 + t_k + t_{k+1} \\ t_0 = t_7. \end{cases} \tag{46}$$

In flat-top SVM, the changes of switch states are arranged as less as possible to reduce the power loss, which means in every switching period v_0 or v_7 can be chosen freely to reduce the number of switch states changes as

$$T = t_k + t_{k+1} + t_0 \text{ or } T = t_k + t_{k+1} + t_7. \tag{47}$$

With the equivalent voltage vector output and different switching sequences, the schematic diagram comparison between classical SVM and flat-top SVM in this article is shown in Fig. 17.

Simulations are provided to show the differences between classical SVM and the flat-top SVM under the same compensation condition. The switch sequences of these two SVM methods are shown as Fig. 18.

Compared with classical SVM in Table XIV, the flat-top SVM can reduce the power loss but with larger THD compensation results. However, the switching frequency is varying for flat-top SVM. Therefore, users can choose SVM methods classical or flat-top based on main demand. The flat-top SVM has lower power loss, whereas classical SVM has better THD performance.

TABLE XIV
COMPARISONS BETWEEN COMPENSATION RESULTS USING CLASSICAL SVM AND FLAT-TOP SVM IN HAPF

	THD after Comp. (%)	PF after Comp.	Power loss (W)
Classical SVM	2.1	1	35.8
Flat-top SVM	3.2	1	26.8

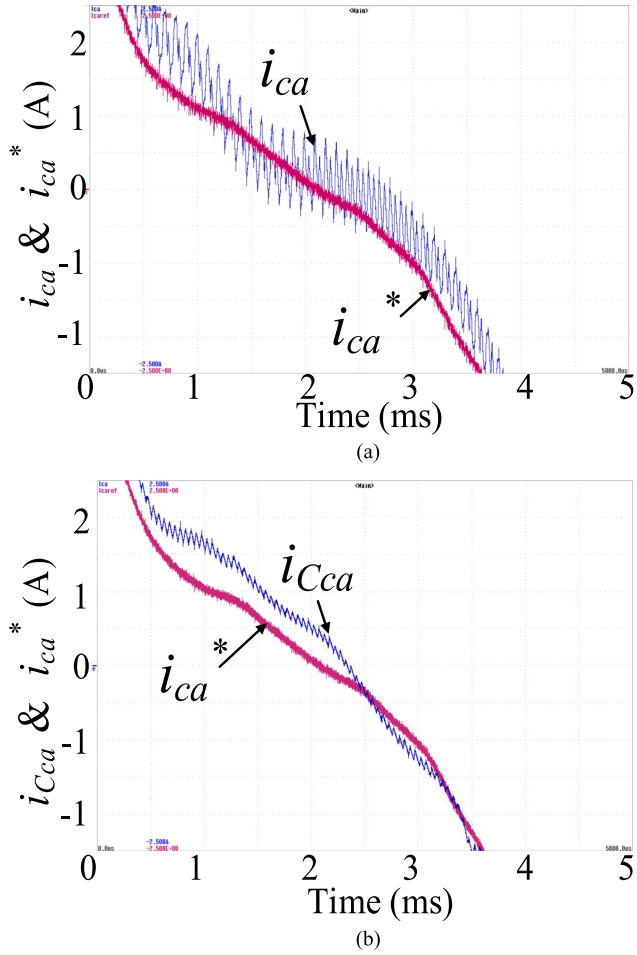

Fig. 19. Zoom-in reference current i_{ca}^* and compensating current i_{ca}/i_{Cca}. (a) APF (10 kHz, coupling 6 mH). (b) HAPF (10 kHz, coupling 6 mH).

C. Relationship Between Compensating and Reference Current in Experiment

It can be seen from Fig. 19, i_{ca} in APF and i_{Cca} in HAPF have been controlled to track their reference i_{ca}^*. Therefore, the source current i_{sx} $(= i_{Lx} - i_{cx})$ can be considered close to the intended compensation result (i_{sx}^*).

APPENDIX

The following Table XV gives the summary for extraction of the article information, which includes the corresponding sections and verifications.

TABLE XV
CONCISE LINKAGES BETWEEN CONCLUSIONS AND RELATED PARTS

Sections	Contents	Verifications
Section II	Circuits and function	Fig. 11, Fig. 13, Table X, Table XI
Section III-A	Injected current in a switching period	Fig. 5, Fig. 9, Fig. 10
Section III-B	Equivalent dc voltage	Fig. 7, Fig. 13, Table X, Table XI
Section III-C	Switching frequency influence	Fig. 9, Fig. 11
Section III-D	Error	Fig. 13, Table X, Table XI
Section III-E	Power loss	Table VIII, Table X, Table XI
Section III-F	Tracking ability	Fig. 13,Fig. 14, Table X, Table XI
Section III-D and -F	Coupling inductor influence	Fig. 13, Fig. 14, Table X, Table XI

REFERENCES

[1] B. Chen, G. Pin, W. M. Ng, T. Parisini, and S.-Y. R. Hui, "A fast-convergent modulation integral observer for online detection of the fundamental and harmonics in grid-connected power electronics systems," *IEEE Trans. Power Electron.*, vol. 32, no. 4, pp. 2596–2607, Apr. 2017.

[2] Q. Wei, L. Xing, D. Xu, B. Wu, and N. R. Zargari, "Modulation schemes for medium-voltage PWM current source converter-based drives: An overview," *IEEE J. Emerg. Select. Top. Power Electron.*, vol. 7, no. 2, pp. 1152–1161, Jun. 2019.

[3] B. Zhao, Q. Yu, and W. Sun, "Extended-phase-shift control of isolated bidirectional dc–dc converter for power distribution in microgrid," *IEEE Trans. Power Electron.*, vol. 27, no. 11, pp. 4667–4680, Nov. 2012

[4] H. Shi *et al.*, "Minimum-backflow-power scheme of DAB-based solid-state transformer with extended-phase-shift control," *IEEE Trans. Ind. Appl.*, vol. 54, no. 4, pp. 1294–1301, Jul./Aug. 2018.

[5] H. Yan, Y. Xu, F. Cai, H. Zhang, W. Zhao, and C. Gerada, "PWM-VSI fault diagnosis for a PMSM drive based on the fuzzy logic approach," *IEEE Trans. Power Electron.*, vol. 34, no. 1, pp. 759–768, Jan. 2019.

[6] G. Xu, D. Sha, Y. Xu, and X. Liao, "Dual-transformer-based DAB converter with wide ZVS range for wide voltage conversion gain application," *IEEE Trans. Ind. Electron.*, vol. 65, no. 4, pp. 3306–3316, Apr. 2018.

[7] V. S.-P. Cheung, R. S.-C. Yeung, H. S.-H. Chung, A. W.-L. Lo, and W. Wu, "A transformer-less unified power quality conditioner with fast dynamic control," *IEEE Trans. Power Electron.*, vol. 33, no. 5, pp. 3926–3937, May 2018.

[8] A. Fereidouni, M. A. S. Masoum, and K. M. Smedley, "Supervisory nearly constant frequency hysteresis current control for active power filter applications in stationary reference frame," *IEEE Power Energy Technol. Syst. J.*, vol. 3, no. 1, pp. 1–12, Mar. 2016.

[9] N. M. Ismail and M. K. Mishra, "Study on the design and switching dynamics of hysteresis current controlled four-leg voltage source inverter for load compensation," *IET Power Electron.*, vol. 11, no. 2, pp. 310–319, Feb. 2018.

[10] M. Siami, D. A. Khaburi, M. Rivera, and J. Rodriguez, "An experimental evaluation of predictive current control and predictive torque control for a PMSM fed by a matrix converter," *IEEE Trans. Ind. Electron.*, vol. 64, no. 11, pp. 8459–8471, Nov. 2017.

[11] W. Jiang, X. Ding, Y. Ni, J. Wang, L. Wang, and W. Ma, "An improved deadbeat control for a three-phase three-line active power filter with current-tracking error compensation," *IEEE Trans. Power Electron.*, vol. 33, no. 3, pp. 2061–2072, Mar. 2018.

[12] M.-C. Wong, Z.-Y. Zhao, Y.-D. Han, and L.-B. Zhao, "Three-dimensional pulse-width modulation technique in three-level power inverters for three-phase four-wired system," *IEEE Trans. Power Electron.*, vol. 16, no. 3, pp. 418–427, May 2001.

[13] M.-C. Wong, J. Tang, and Y.-D. Han, "Cylindrical coordinate control of three-dimensional PWM technique in three-phase four-wired trilevel inverter," *IEEE Trans. Power Electron.*, vol. 18, no. 1, pp. 208–220, Jan. 2003.

[14] H. W. Van der Broeck, H.-C. Skudelny, and G. V. Stanke, "Analysis and realization of a pulsewidth modulator based on voltage space vectors," *IEEE Trans. Ind. Appl.*, vol. 24, no. 1, pp. 142–150, Jan./Feb. 1988.

[15] S. Engel, K. Rigbers, and R. W. De Doncker, "Digital repetitive control of a three-phase flat-top-modulated grid tie solar inverter," in *Proc. 13th Eur. Conf. Power Electron. Appl.*, 2009, pp. 1–10.

[16] L. Wang *et al.*, "Non-linear adaptive hysteresis band pulse-width modulation control for hybrid active power filters to reduce switching loss," *IET Power Electron*., vol. 8, no. 11, pp. 2156–2167, Nov. 2015.

[17] C.-S. Lam, M.-C. Wong, and Y.-D. Han, "Hysteresis current control of hybrid active power filter," *IET Power Electron*., vol. 5, no. 7, pp. 1175–1187, Aug. 2012.

[18] W.-K. Sou *et al.*, "A deadbeat current controller of LC-hybrid active power filter for power quality improvement," *IEEE J. Trans. Emerg. Sel. Top. Power Electron.*, to be published.

[19] N. Y. Dai, W. C. Zhang, M. C. Wong, J. M. Guerrero, and C. S. Lam, "Analysis, control and experimental verification of a single-phase capacitivecoupling grid-connected inverter," *IET Power Electron.*, vol. 8, no. 5, pp. 770–782, May 2015.

[20] L. Wang, C.-S. Lam, and M.-C. Wong, "Modeling and parameter design of thyristor-controlled LC-coupled hybrid active power filter (TCLC-HAPF) for unbalanced compensation," *IEEE Trans. Ind. Electron.*, vol. 64, no. 3, pp. 1827–1840, Mar. 2017.

[21] L. Wang, C. S. Lam and M. C. Wong, "Hybrid structure of static var compensator and hybrid active power filter (SVC//HAPF) for medium voltage heavy loads compensation," *IEEE Trans. Ind. Electron.*, vol. 65, no. 6, pp. 4432–4442, Jun. 2018

[22] B. Singh, K. Al-Haddad, and A. Chandra, "A review of active filters for power quality improvement," *IEEE Trans. Ind. Electron.*, vol. 46, no. 5, pp. 960–971, Oct. 1999.

[23] M. El-Habrouk, M. K. Darwish, and P. Mehta, "Active power filters: A review," *Proc. IEE—Elect. Power Appl.*, vol. 147, no. 5, pp. 403–413, Sep. 2000.

[24] H. Akagi, S. Srianthumrong, and Y. Tamai, "Comparisons in circuit configuration and filtering performance between hybrid and pure shunt active filters," in *Proc. IAS Annu. Meeting Conf. Rec. Industry Appl. Conf.*, 2003, vol. 2, pp. 1195–1202.

[25] L. Chen, Y. Xie, and Z. Zhang, "Comparison of hybrid active power filter topologies and principles," in *Proc. Int. Conf. Elect. Mach. Syst.*, Oct. 17–20, 2008, pp. 2030—2035.

[26] Y. Pal, A. Swarup, and B. Singh, "A review of compensating type custom power devices for power quality improvement," in *Proc. Joint Int. Conf. Power Syst. Technol. IEEE Power India Conf.*, 2008, pp. 1–8.

[27] T. Demirdelen, M. Inci, K. C. Bayindir, and M. Tumay, "Review of hybrid active power filter topologies and controllers," in *Proc. IEEE 4th Int. Conf. Power Eng. , Energy Elect. Drives*, May 2013, pp. 587–592.

[28] Y.-W. Wang, M.-C. Wong, and C.-S. Lam, "Historical review of parallel hybrid active power filter for power quality improvement," in *Proc. TENCON Conf. Convergent Technol. Asia-Pacific Region*, Nov. 2015.

[29] L. Wang, C.-S. Lam, and M.-C. Wong, "The analysis of DC voltage, compensation range, cost, reliability and power loss for shunt (Hybrid) active power filters," in *Proc. Asia-Pacific Power Energy Eng. Conf.*, Oct. 2018, pp. 640–645.

[30] C. Venkatesh, D. Srikanth Kumar, D. V. S. S. Siva Sarma, and M. Sydulu, "Modelling of nonlinear loads and estimation of harmonics in industrial distribution system," in *Proc. 15th Nat. Power Syst. Conf.*, Dec. 2008, pp. 592–597.

[31] C. Batard, F. Poitiers, C. Millet, and N. Ginot, "Simulation of power converters using matlab-simulink," in *MATLAB: A Fundamental Tool for Scientific Computing and Eng.ineering Applications*, vol. 1, Vasilios Katsikis, Ed., Rijeka, Croatia: In Tech, 2012.

[32] N. S. Preda, I. I. Incze, M. Imecs, and Cs. Szabo, "Flat-Top space-vector modulation implemented on a fixed-point DSP," in *Proc. 5th Int. Symp. Appl. Comput. Intell. Informat.*, May, 2009, pp. 153–158.

[33] J. Lee, J. Choi, and Y. Nishida, "Overmodulation strategy of NPC type 3-level inverter for traction drives," in *Proc. 7th Int. Conf. Power Electron.*, 2007, pp. 137–142.

[34] R. Burgos and E. Wiechmann, "Extended voltage swell ride-through capability for PWM voltage-source rectifiers," *IEEE Trans. Ind. Electron.*, vol. 52, no. 4, pp. 1086–1098, Aug. 2003.

[35] L. Wang, C.-S. Lam, and M.-C. Wong, "Minimizing inverter capacity design and comparative performance evaluation of SVC-coupling hybrid active power filters," *IEEE Trans. Power Electron.*, vol. 34, no. 2, pp. 1227–1242, Feb. 2019.

[36] K. Takagi and H. Fujita, "A three-phase grid-connected inverter equipped with a shunt instantaneous reactive power compensator," *IEEE Trans. Ind. Appl.*, vol. 55, no. 4, pp. 3955–3966, Jul./Aug. 2019.

[37] A. K. Yadav *et al.*, "A hybrid 7-level inverter using low-voltage devices and operation with single DC-link," *IEEE Trans. Power Electron.*, vol. 34, no. 10, pp. 9844–9853, Oct. 2019.

Man-Chung Wong (Senior Member, IEEE) received the B.Sc. and M.Sc. degrees in electrical and electronics engineering from the University of Macau, Macao, China, in 1993 and 1997, respectively, and the Ph.D. degree in electrical engineering from Tsinghua University, Beijing, China, in 2003.

Currently, he is a Professor with the Department of Electrical and Computer Engineering, University of Macau. He was a Visiting Fellow with the Cambridge University, Cambridge, U.K. He is also affiliated with the State Key Laboratory of Internet of Things for Smart City and Sate Key Laboratory of Analog and Mixed Signal VLSI, University of Macau. Since 2017, he is the Head of the Department of Electrical and Computer Engineering, Faculty of Science and Technology (FST), University of Macau. He has authored and coauthored four books and more than 150 technical journals and conference papers. He holds four U.S. patent and eight Chinese patents. His research interests include integrated power electronics controllers, power electronics converters, power quality compensators, renewable energy, wireless power transfer, and smart grids.

Prof. Wong was the recipient of Macao Science and Technology Invention Awards (Second Class at 2018 and Third Class at 2014 and 2012) and Young Scientist Award from Insituto Internacional De Macau, in 2000, Young Scholar Award from University of Macau, in 2001, and Second Prize of the 2003 Tsinghua University Excellent Doctor Thesis Award. He was IEEE Region 10 Conference TENCON Macao 2015 General Chair and IEEE APPEEC Macao 2019 General Chair. He was Chair of IEEE Macau Section, from 2014 to 2015. He is currently the Chair of IEEE Macau PES/Power Electronics Society (PELS) Joint Chapter and has been the IEEE Region 10 Power and Energy Society North Representative since 2015.

Ying Pang (Student Member, IEEE) received the B.Sc. degree in electrical engineering from Southwest Jiaotong University, Chengdu, China, in 2015, and the M.Sc. degree in electrical and computer engineering in 2018 from the University of Macau, Macao, where he is currently working toward the Ph.D. degree in electrical and computer engineering with the State Key Laboratory of Internet of Things for Smart City.

His research interests include power filter, smart grid, renewable energy, and distributed generation.

Zeng Xiang (Member, IEEE) received the B.Sc. degree in electrical engineering and automation from the Tianjin University of Science and Technology, Tianjin, China, in 2009, and the M.Sc. degree in electronic engineering from Hunan University, Changsha, China, in 2012. He is currently working toward the Ph.D. degree in electrical and computer engineering with the State Key Laboratory of Internet of Things for Smart City, University of Macau, Macau.

From 2012 to 2015, he was an R&D Engineer with Zhuhai Wanlida Electrical Automation Co., Ltd., Zhuhai, China. His research interests include high-performance converters for microgrids, power quality, and distributed power generation systems.

Lei Wang (Senior Member, IEEE) received the B.Sc. degree in electrical and electronics engineering from the University of Macau (UM), Macao, China, in 2011, the M.Sc. degree in electronics engineering from the Hong Kong University of Science and Technology (HKUST), Hong Kong, in 2012, and the Ph.D. degree in electrical and computer engineering from the UM, in 2017.

He was a Postdoctoral Fellow with the Power Electronics Laboratory of UM, from January 2017 to February 2019. He was a Visiting Fellow with the Department of Electrical and Computer Engineering, University of Auckland, Auckland, New Zealand, from February 2019 to August 2019. In 2019, he joined College of Electrical and Information Engineering, Hunan University, Changsha, China, where he is currently a Full Professor. He has authored one Springer book, one Elsevier book chapter, five patents (U.S.A and China), and over 30 journal and conference papers.

Dr. Wang was the recipient of the Champion Award in the "Schneider Electric Energy Efficiency Cup", Hong Kong, 2011, and the Macao Science and Technology R&D Award for Postgraduates (Ph.D), in 2018.

Chi-Seng Lam (Senior Member, IEEE) received the Ph.D. degree in electrical and electronics engineering from the University of Macau (UM), Macao, China, in 2012. He completed the Clare Hall Study Programme at the University of Cambridge, Cambridge, U.K., in 2019.

From 2006 to 2009, he was an Electrical and Mechanical Engineer with UM, where he worked as a Laboratory Technician from 2009 to 2012. He was a Postdoctoral Fellow with The Hong Kong Polytechnic University, Hong Kong, China, in 2013. He is currently an Associate Professor with the State Key Laboratory of Analog and Mixed-Signal VLSI and the Institute of Microelectronics, UM, and also with the Department of Electrical and Computer Engineering, Faculty of Science and Technology, UM. He has coauthored or coedited four books and more than 110 technical journals and conference papers. He holds four U.S. and two Chinese patents. His research interests include power quality compensators, renewable energy generation, integrated power electronics controllers, power management integrated circuits, and wireless power transfer.

Dr. Lam serves/served as a member for the Organizing Committee or Technical Program Committee of IEEE international conferences, including Annual Conference of the IEEE Industrial Electronics Society (IECON) 2020, IECON 2019, IEEE Asian Solid-State Circuits Conference (ASSCC) 2019, Asia-Pacific Power & Energy Engineering Conference (APPEEC) 2019, IECON 2018, International Conference on Industrial Electronics for Sustainable Energy Systems (IESES0 2018, Asia and South Pacific Design Automation Conference (ASP-DAC) 2016, and International Technical Conference (TENCON) 2015. He was the recipient or co-recipient of the IEEE Power Electronics Society (PES) Chapter Outstanding Engineer Award, in 2016, the Best Track Paper Award of APPEEC 2019, the Best Paper Award of Integrated Circuits, Technologies and Applications (ICTA) 2019, the Merit Paper Award of the 3rd Regional Inter-University Postgraduate Electrical and Electronic Engineering Conference (RIUPEEEC) Conference, in 2005, the Macao Science and Technology Invention Award (Second Class and Third Class), in 2018 and 2014, respectively, and the Research and Development Award for Postgraduates (Ph.D.), in 2012. He was the Vice-Chair of the IEEE Macau Section, from 2016 to 2020, and the Chair of the IEEE Macau CAS Chapter, from 2017 to 2018. He is currently the Chair of the IEEE Macau IES Chapter and the Power Quality Subcommittee Chair of the IEEE IES Technical Committee on Power Electronics. He currently serves as an Associate Editor for IEEE TRANSACTIONS ON INDUSTRIAL ELECTRONICS and IEEE ACCESS, and a Guest Editor for the IEEE TRANSACTIONS ON CIRCUITS AND SYSTEMS II: EXPRESS BRIEFS and the IET POWER ELECTRONICS.